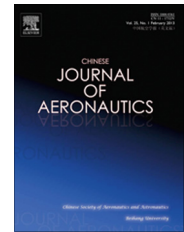




Chinese Society of Aeronautics and Astronautics  
& Beihang University

Chinese Journal of Aeronautics

cja@buaa.edu.cn  
www.sciencedirect.com



# Horn–Schunck optical flow applied to deformation measurement of a birdlike airfoil



Gong Xiaoliang<sup>a,\*</sup>, Stephan Bansmer<sup>b</sup>

<sup>a</sup> School of Aeronautics, Northwestern Polytechnical University, Xi'an 710072, China

<sup>b</sup> Institute of Fluid Mechanics, Technische Universität Braunschweig, Braunschweig 38108, Germany

Received 16 October 2014; revised 20 April 2015; accepted 11 May 2015

Available online 2 September 2015

## KEYWORDS

Deformation measurements;  
Flexible airfoil;  
Horn–Schunck;  
Optical flow;  
Stereoscopic

**Abstract** Current deformation measurement techniques suffer from limited spatial resolution. In this work, a highly accurate and high-resolution Horn–Schunck optical flow method is developed and then applied to measuring the static deformation of a birdlike flexible airfoil at a series of angles of attack at Reynolds number 100,000 in a low speed, low noise wind tunnel. To allow relatively large displacements, a nonlinear Horn–Schunck model and a coarse-to-fine warping process are adopted. To preserve optical flow discontinuities, a nonquadratic penalization function, a multi-cue driven bilateral filtering and a principle component analysis of local image patterns are used. First, the accuracy and convergence of this Horn–Schunck technique are verified on a benchmark. Then, the maximum displacement that can be reliably calculated by this technique is studied on synthetic images. Both studies are compared with the performance of a Lucas–Kanade optical flow method. Finally, the Horn–Schunck technique is used to estimate the 3-D deformation of the birdlike airfoil through a stereoscopic camera setup. The results are compared with those computed by Lucas–Kanade optical flow, image correlation and numerical simulation.

© 2015 The Authors. Production and hosting by Elsevier Ltd. on behalf of CSAA & BUAA. This is an open access article under the CC BY-NC-ND license (<http://creativecommons.org/licenses/by-nc-nd/4.0/>).

## 1. Introduction

For the past few decades, many questions about natural flying mechanisms found in birds and insects remain open even though there has been continuous and substantial research in the matter through theoretical, experimental and numerical

results in flapping flight. One example is how aerodynamic forces, elastic forces and inertial forces interact with each other during different flapping phases (e.g., plunging and pitching) when the wings deform significantly. To reveal the hidden mechanism behind this aeroelastic interaction, the deformation of the flexible wing should be measured as precisely as possible. The history of optical measurements of the deformation of the wing of an aircraft model in the wind tunnel can be dated back to the 1970s when photogrammetry<sup>1</sup> was first introduced and evaluated. The dynamic counterpart of photogrammetry is videogrammetry which is applied to a series of images taken sequentially at high rate, providing a proper means of studying the motion of the object as a function of time.<sup>2</sup> Accurate photogrammetry requires high contrast surface features on the

\* Corresponding author. Tel.: +86 29 88494356.

E-mail address: [xlianggong@gmail.com](mailto:xlianggong@gmail.com) (X. Gong).

Peer review under responsibility of Editorial Committee of CJA.



Production and hosting by Elsevier

measured object. Normally, painted-on targets<sup>3</sup> or retro-reflective tape targets<sup>4</sup> are placed at the locations where the deformation data is required. In situations where there are restrictions on those attached physical targets, the natural identifiable patterns on the wings<sup>5</sup> or projected patterns<sup>6</sup> serve as alternative choices. The primary disadvantage of photogrammetry is the lack of deformation data over the entire captured surface, leading to the use of deformation data at sparse points and accordingly interpolated data.<sup>7</sup> Another widely used method is moiré and fringe projection interferometry (MFPI) that was initially introduced in 1995 by German Aerospace Research Center DLR in the transonic wind tunnel Göttingen to quantitatively measure the bending and twist deformations of the wing.<sup>8</sup> MFPI uses the projection of a fringe pattern or grating to measure the topology of a given surface. Although less accurate than photogrammetry, MFPI reveals the full-field object shape and deformation. The main drawback of MFPI is that despite the ability to measure the out-of-plane model shape and deformation, it encounters a huge challenge when tracking the in-plane motion.<sup>9</sup> The third method is image correlation. The underlying principle is to track the motion of the random speckling patterns on the surface by analyzing the displacement of the patterns within discretized subsets (interrogation windows). The displacement in each window can be found by maximizing a correlation function.<sup>10</sup> Image correlation has only recently become increasingly popular.<sup>11</sup> It has been proved to be much more robust and provides greater dynamic range than many other full-field imaging techniques such as MFPI,<sup>12</sup> and has competitively high accuracy compared to traditional strain gages,<sup>13</sup> laser displacement sensors,<sup>14</sup> and target-based photogrammetry.<sup>15</sup> In spite of all this, image correlation has drawbacks. The main one is that the spatial resolution is confined by the interrogation window size. The task of this paper is to explore a powerful method that possesses higher spatial resolution than image correlation while preserving the high accuracy. Optical flow is very likely to challenge image correlation in this case. Optical flow calculates the velocity field of pattern motions in 2-D images. It is an effective technique to track the motion of an object. For example, optical flow has been used to detect human movements, navigate vehicles, and measure surface strain, plant growth, and flow motion. Nevertheless, optical flow has rarely been applied to measuring the deformation of aircraft or wings in wind tunnels. The main reason lies in the fact that those mentioned techniques are well developed and perform well.

Actually, there is a close relationship between optical flow and image correlation. According to the categorization of different optical flow methods by Barron et al.,<sup>16</sup> the Horn-Schunck (HS) optical flow is a differential technique that has higher spatial resolution, while the image correlation is a region-based matching method that is more robust against noise. Optical flow is usually classified into two categories: global methods based on the HS scheme<sup>17</sup> and local methods based on the Lucas-Kanade (LK) scheme.<sup>18</sup> Both methods are based on the same assumption that the pixel value (image intensity or brightness) of moving patterns does not change over a short displacement. This is known as the intensity constancy assumption. To calculate the velocity field of moving patterns, apart from this assumption, more constraints are required. HS scheme assumes that the velocity field varies globally smoothly and neighboring pixels have almost the

same velocity, while LK scheme assumes that the velocity field keeps locally constant and neighboring pixels in one interrogation window share the same motion. As a result, HS generates a dense velocity field and it is sensitive to outliers and noise, while LK generates a relatively sparser velocity field but it offers high robustness under outliers and noise.<sup>19</sup> Recently, LK optical flow method has been applied to the static deformation measurements of a birdlike airfoil in a wind tunnel experiment by Gong et al.<sup>20</sup> The results of LK clearly manifest higher spatial resolution than those of image correlation and displayed high accuracy at the same time. In this paper, we intend to expand their work and study the possibility of HS optical flow method to measure the deformation of a birdlike airfoil.

## 2. Horn-Schunck optical flow

Since Horn and Schunck proposed their famous method in 1981<sup>17</sup>, many researches have been trying to overcome the drawbacks of this method and improve its robustness and accuracy, which is clearly demonstrated by the results on the Middlebury optical flow benchmark.<sup>21</sup> In the rest of this section, first, the original HS method will be briefly discussed. Then, specific techniques to improve the original method will be introduced.

Let  $I_1(X, Y, t)$  denote the two-dimensional image intensity, where  $X$  and  $Y$  describe the location of a pixel in image coordinates and  $t$  is the time. Let  $I_2(X + dX, Y + dY, t + dt)$  denote the pixel intensity after a short time duration  $dt$ , where  $dX, dY$  are the displacements of this pixel in the image. The fundamental assumption of optical flow is that the intensity of a pixel is not changed by the displacement. This intensity constancy could be described mathematically as follows:

$$I_1(X, Y, t) = I_2(X + dX, Y + dY, t + dt) \quad (1)$$

By performing a first-order Taylor expansion on  $I_2$ , with velocity  $U = dX/dt$ ,  $V = dY/dt$ , and denoting partial derivatives of the image intensity as  $I_X, I_Y, I_t$ , we have the linearized version of intensity constancy assumption:

$$I_X U + I_Y V + I_t = 0 \quad (2)$$

Eq. (2) is the famous optical flow equation.<sup>17</sup> Since  $U$  and  $V$  are two unknowns, this equation system is underdetermined, which is also the well-known aperture problem. To solve this problem, first, HS adds a global constraint that penalizes the global deviation from the intensity constancy assumption, which is defined by the following energy functional:

$$E_D(U, V) = \int_{\Omega} \varphi((I_X U + I_Y V + I_t)^2) d\Omega \quad (3)$$

Second, HS adds an extra global constraint that penalizes the total variation of the flow field, which is defined by the following energy functional:

$$E_S(U, V) = \int_{\Omega} (\varphi(U_X^2) + \varphi(U_Y^2) + \varphi(V_X^2) + \varphi(V_Y^2)) d\Omega \quad (4)$$

where  $E_D$  is commonly called the data term,  $E_S$  is commonly called the smoothness term. The smoothness constraint is expressed in the gradient of the optical flow velocity, which is reasonable because the velocities of neighboring pixels vary smoothly except at the boundaries of objects in the scene.

Here,  $\varphi$  is the penalty function and  $\Omega$  the image spatial domain. In the original HS method, the authors used the quadratic penalty  $\varphi(s^2) = s^2$ . Assembling the data term from Eq. (3) and smoothness term from Eq. (4) yields the total energy functional  $E$ :

$$E(U, V) = E_D + \beta E_S \quad (5)$$

Here,  $\beta$  is a weighting factor ( $\beta > 0$ ). Applying a proper minimization method on  $E(U, V)$ , the flow field can be retrieved.

### 2.1. Improvements of original HS model

As proved by many later researchers, there are mainly three drawbacks of the original HS model. First, the linearization of Eq. (1) maintains accurate only for quite small displacements. This issue was first addressed by Nagel<sup>22</sup> and a new nonlinear data term was introduced as follows:

$$E_D(U, V) = \int_{\Omega} \varphi((I_2(X + dX, Y + dY, t + dt) - I_1(X, Y, t))^2) d\Omega \quad (6)$$

This new nonlinear data term was later proved capable of capturing larger displacements with higher accuracy and it remains most widely used. This paper uses this new data term from Eq. (6) together with aforementioned smoothness term in Eq. (4) to form the total energy functional shown in Eq. (5).

The second drawback of the original HS model lies in the quadratic penalty. As discussed by Black and Anandan,<sup>23</sup> the quadratic estimator is susceptible to outliers, which is one important reason for the erroneous estimation of the optical flow across motion boundaries, thus leading to an over-smooth boundary. In contrast, the  $L^1$  norm,  $\varphi(s^2) = |s|$ , allows to preserve sharp discontinuities. The integral of the  $L^1$  norm is referred to as the total variation. The successful applications of the  $L^1$  norm in optical flow have been demonstrated by many researchers.<sup>24,25</sup> In this paper, a differentiable approximation of the  $L^1$  norm  $\varphi(s^2) = \sqrt{s^2 + \epsilon^2}$  was used. The parameter  $\epsilon$  is a small constant only for numerical reasons. We set  $\epsilon = 0.001$ , the same as that by Brox et al.<sup>24</sup>

The third defect of the original HS model is that because the smoothness term is applied indiscriminately across the whole image, even with the introduction of the discontinuity-preserving  $L^1$  norm, the resulting flow field often shows over-smoothing across motion boundaries. To solve this problem, inspired by the work of Brox and Weickert,<sup>26</sup> a flow-driven or image-driven anisotropic diffusion tensor (smoothing data along a boundary rather than across it) could be used to replace the smoothness term (homogenous smoothing). In this case, as demonstrated by Xiao et al.,<sup>27</sup> the minimization of the total energy could be separated into a two-step procedure: (A) calculating an intermediate optical flow field  $\tilde{V}$ ; (B) applying an independent diffusion on the intermediate flow field. Then, the anisotropic diffusion can be substituted by a more flexible oriented Gaussian filter that does not need traditional PDE iteration anymore. At occluded regions, when performing the oriented Gaussian filter only within the region where the kernel central pixel is therein, the resulting flow field is more accurate than that of the traditional anisotropic diffusion that unavoidably takes in some flow information from inconsistent regions despite the smoothing (diffusion) being

stretched along the motion boundary.<sup>27</sup> Because different Gaussian filters can be simply concatenated by convolution operation, it is much more straightforward to include Gaussian filters representing spatial distance, image similarity, and motion similarity into one filter  $W$ :<sup>27</sup>

$$W = RG_{\Omega}(\Omega, \sigma_{\Omega})G_I(I, \sigma_I)G_{\tilde{V}}(\tilde{V}, \sigma_{\tilde{V}}) \quad (7)$$

where  $R$  denotes the occlusion labeling,  $G_{\Omega}(\Omega, \sigma_{\Omega})$  a Gaussian kernel on image spatial domain  $\Omega$  with variance  $\sigma_{\Omega}$ ,  $G_I(I, \sigma_I)$  a Gaussian kernel on image intensity domain  $I$  with variance  $\sigma_I$ , and  $G_{\tilde{V}}(\tilde{V}, \sigma_{\tilde{V}})$  a Gaussian kernel on intermediate flow velocity domain  $\tilde{V}$  with variance  $\sigma_{\tilde{V}}$ . The occlusion labeling  $R$  calculated by Xiao et al.<sup>27</sup> is based on checking the squared image intensity difference between two sequential images, which is not reliable because the motion boundary and image intensity boundary may not coincide. In this paper,  $R$  is calculated according to the flow-divergence-difference-based method.<sup>28</sup>

Finally, if we convolute  $\tilde{V}$  by  $W$ , the desired flow field can be generated by this weighted average filtering.<sup>27,28</sup> However, a better approach is to apply a weighted median filter that inherits edge preservation and efficient noise attenuation of the median filter.<sup>29</sup> Median filtering of intermediate flow fields has been proved to be very effective to improve accuracy. This paper carries out a fast version of weighted median filtering proposed by Sun et al.<sup>30</sup>

### 2.2. Improvements of minimizations of original HS

Apart from some defects in the model, the old minimization method is also responsible for inaccurate results of original HS. In this paper, the minimization of total energy  $E(U, V)$  was carried out according to the famous warping-based method proposed by Brox et al.<sup>24</sup> The main contribution of his method is to postpone the linearization to the numerical scheme. The original HS estimated spatial derivatives of image intensity by first-order difference which is obviously not accurate enough. This paper took a five-point central difference stencil  $1/12[-1, 8, 0, -8, 1]$  that was suggested by Barron et al.<sup>16</sup> Like original HS, the final spatial derivatives were calculated by the temporal average of spatial derivatives of two sequential images. The only difference is that in this paper the spatial derivatives on the second image were estimated on the warped image that was generated during the coarse-to-fine warping process. This process consists of the optical flow calculation on pyramidal images and the cubic-interpolation-based warping, which has been generally recognized as a high performance technique, especially for large displacements.<sup>24</sup> Pyramidal images were multi-scale images which were acquired by continuously calculating Gaussian pyramid reduction of the full resolution image. The reduction factor was 0.5. The number of pyramid levels was adaptively determined so that each dimension of the coarsest image was around 30 pixels.<sup>31</sup> Computations started from the coarsest image, and then went to the next finer image, until finally solved the optical flow of the full resolution image. At each pyramidal level, an inner warping iteration was performed to refine the optical flow.

It is well-known that the flow fields at textureless regions (the data term vanishes) are generated by the fill-in process induced by the smoothness term. If the textureless region is surrounded by the similar-motion-belonged textured region,

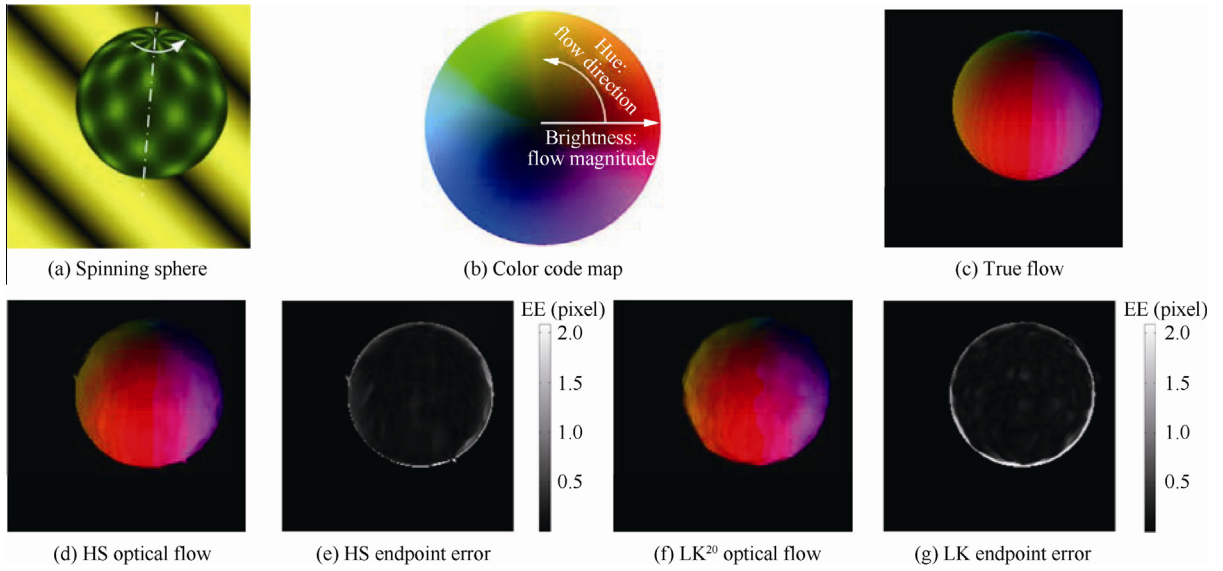


Fig. 1 Optical flow of spinning sphere.

this fill-in process helps to generate a full density optical flow field. Otherwise, an erroneous flow field at the textureless region may be induced. In the experiments of this paper, because the textured object moved on a static textureless background, the textureless region could be easily identified by measuring the smaller eigenvalue of the local image intensity structure tensor. As Gong et al. did in their work,<sup>20</sup> if the smaller eigenvalue was less than 1, the velocity was set to zero.

### 3. Validation of HS optical flow

#### 3.1. LK optical flow

To validate the HS optical flow code, both accuracy and convergence of HS optical flow results were studied in comparison with LK optical flow studied by Gong et al.<sup>20</sup> LK optical flow minimizes the sum of the squared error between  $I_1(X, Y, t)$  and  $I_2(X + dX, Y + dY, t + dt)$  in an integration window  $w$ . After linearization is done in Eq. (2), a total energy is generated:

$$E(U, V) = \sum_{X, Y \in w} (I_x U + I_y V + I_t)^2 \quad (8)$$

The minimization of  $E$  in Eq. (8) leads to a linear system where  $U$  and  $V$  can be resolved. The LK used by Gong et al. also took advantage of coarse-to-fine warping and pyramidal scheme. Apart from that, nonlinear structure tensor diffusion was used to preserve motion discontinuity.

#### 3.2. Spinning sphere

To compare the results of HS to the results of LK, the validation here was carried out on the same two image sequences used for LK. The first one is the synthetic sphere sequence.<sup>32</sup> A textured sphere is spinning in a static striped background, see Fig. 1(a). All color images were converted into grayscale images, because black and white photos were used in experiments. The three parameters of bilateral filtering were set

according to experience to be:  $\sigma_\Omega = 7$ ,  $\sigma_I = 3$ ,  $\sigma_V = 4$ . The inner iteration step for warping was 20. The result is shown by the color coded map in Fig. 1(d). The velocity orientation and magnitude are represented by the hue and brightness in the color wheel shown in Fig. 1(b), respectively. Obviously, the HS optical flow result preserved a much sharper motion discontinuity than the LK optical flow result (see Fig. 1(f)). When comparing sphere optical flow with true flow (see Fig. 1(c)), the advantage of HS in preservation of the sphere boundary is even more clear (see Fig. 1(e) and (g)).

The error image was measured in endpoint error (EE). EE is calculated by measuring the flow difference between the optical flow  $V = [U, V, 1]$  and the true flow  $V_t = [U_t, V_t, 1]$ .

$$EE = \sqrt{(U - U_t)^2 + (V - V_t)^2} \quad (9)$$

To further understand this difference quantitatively, a 3-pixel-width annular region was defined on the sphere boundary. The average EEs of HS and LK within this annular region were 0.66 pixel and 1.10 pixels, respectively while the average EE of HS and LK within the sphere were equally 0.1 pixel.

The above discussion seems to convince that the HS, compared to LK, achieved the same performance in non-occlusion region (within the sphere). However, examining the optical flow result carefully reveals the fact that the optical flow of HS (see Fig. 1(d)) retrieved a more clear longitude line than that of LK (see Fig. 1(f)). This difference cannot be illustrated by the average EE, which will be discovered by some other error measurements.

Generally, apart from EE, two other ways to validate the optical flow results are the average angular error (AE) and the standard deviation of angular error (SDAE). AE measures the angular difference between the optical flow  $V$  and the true flow  $V_t$ .

$$AE = \arccos \left( \frac{UU_t + VV_t + 1}{\sqrt{U^2 + V^2 + 1} \sqrt{U_t^2 + V_t^2 + 1}} \right) \quad (10)$$



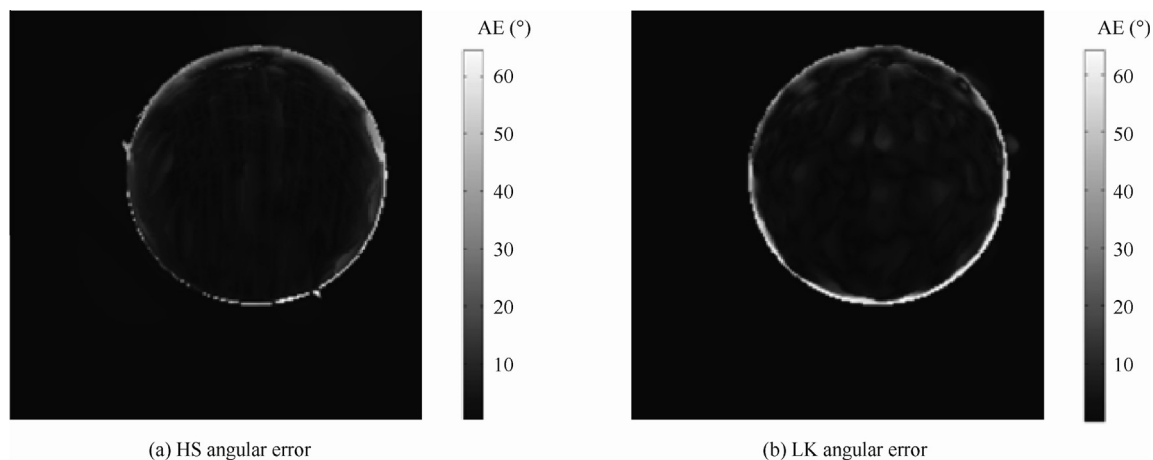


**Fig. 2** Comparison of angular error between HS and LK.

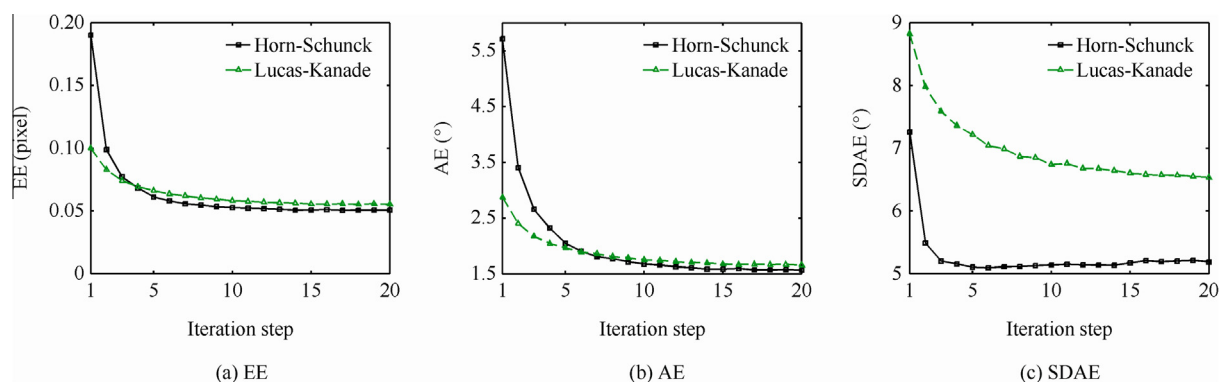


**Fig. 3** Convergence property measured in three methods.

It is noted that large and small velocities were treated without amplification for AE. In contrast, errors of larger velocities measured in EE were weighted more. SDAE is defined as the standard deviation of AE.

Fig. 2 shows angular error images of HS and LK results which are very similar to their corresponding EE images in Fig. 1. Again, big errors appeared on the sphere boundary and HS preserved the boundary better than LK. The average AEs were  $23.1^\circ$  and  $35.6^\circ$  for HS and LK on the sphere boundary, respectively, but equally  $2.6^\circ$  within the sphere.

The convergence property of HS was compared with that of LK through all three measurements, as shown in Fig. 3. As mentioned before, the EE of HS and LK almost converged to the same level (see Fig. 3(a)). It is the same case with AE (see Fig. 3(b)). However, the flow differences of HS and LK are prominently illustrated by SDAE (see Fig. 3(c)). Therefore, the average errors of both methods were similar while the result of HS showed less variation in the flow direction, which is also indicated in Fig. 2. This clarifies why HS captured subtle longitude line in the flow field.

### 3.3. Translating rectangle

The second synthetic image sequence was obtained in order to know the limit of the motion magnitude for the HS method. In the scene, a rectangle with random pattern is translating

towards the right on a static black background (see Fig. 4 (a)). The true flow is shown in Fig. 4(b) by subsampled velocity vectors.

To compare with the result of LK<sup>20</sup>, first the HS optical flow method was applied to displacement from 1 pixel to 6 pixels. All parameters were kept the same as used in the sphere sequence. The EE is shown by a grayscale images in Fig. 5 (a). It is clearly shown in Fig. 5(a) that the effectiveness of HS to preserve flow discontinuity hardly degenerated with the increasing motion displacement from 1 pixel to 6 pixels in great contrast to the obvious deterioration of LK shown in Fig. 5(b). The comparison of EE between HS and LK demonstrates that even when the displacement was 1 pixel, HS optical flow generated a much smaller error than LK optical flow on the motion boundary. The larger the displacement, the greater advantage HS had in preserving the motion boundary.

The previous discussion did not answer what the ultimate limit of the motion displacement calculated by HS optical flow is. To study this, the displacement was increased to 7 pixels. The results were still shown in three measurements, EE, AE and SDAE (see Fig. 6). Again, all the three measurements obviously show that HS generated a more accurate flow field than LK. The errors of HS kept at a rather constant low level from 1 pixel to 6 pixels, while the errors of LK increased linearly from 1 pixel to 3 pixels, showed a jump at 4 pixels, and

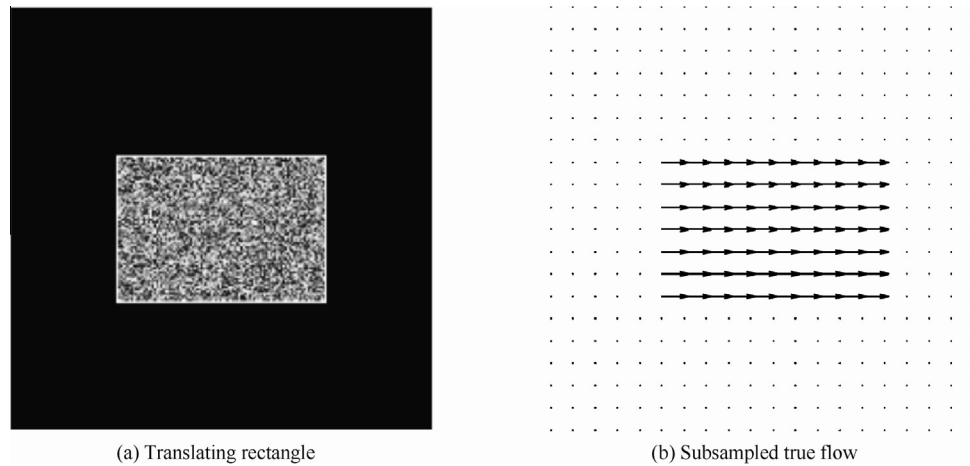


**Fig. 4** Random-pattern-textured translating rectangle.

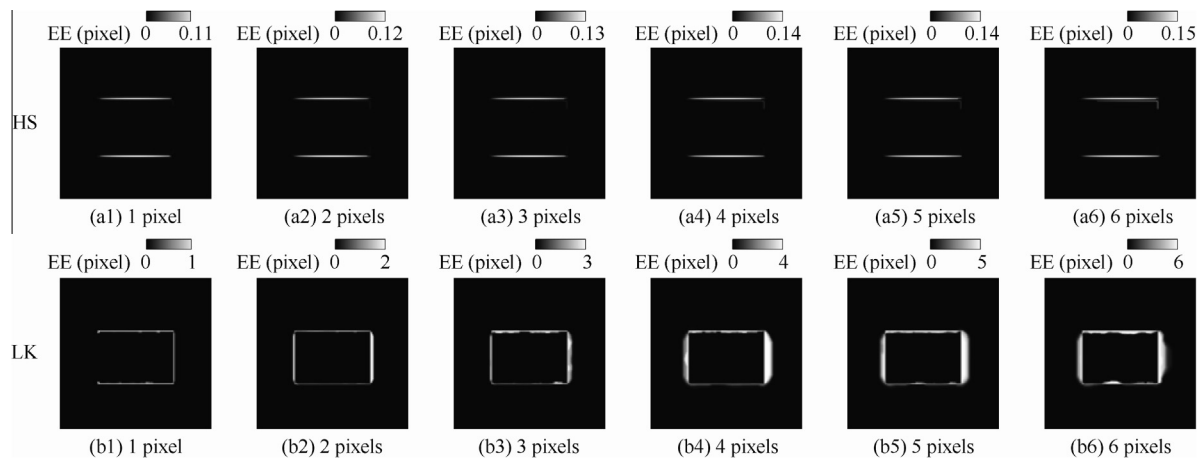


**Fig. 5** Endpoint error for motion from 1 to 6 pixels.

then went up linearly to 6 pixels. Actually, those error curves quantitatively display the variation of grayscale error images shown in Fig. 5, because the biggest errors occurred around the motion boundary in both, HS and LK. Last but not least, errors of both HS and LK increased sharply with the displacement increasing from 6 pixels to 7 pixels. Thus, in the following experiment, as a compromise between motion magnitude and optical flow accuracy, the maximum motion was limited to fewer than 6 pixels, twice the motion limitation of LK.<sup>20</sup>

#### 4. Experimental setup

Wind tunnel experiments of measuring the deformation of the birdlike airfoil were carried out in a low speed, low noise wind tunnel. The airfoil (see Fig. 7) is an advanced version of the flexible birdlike airfoil SG04 presented by Bansmer et al.<sup>33</sup> The wing's dimensions are  $398 \times 200$  mm (span  $\times$  chord). The fore part of the wing is stiff and the rear part of the wing is composed of seven overlapping flexible feather shells. The white upper surface of the wing was sprayed with stochastic black ink patterns. To measure 3-D deformation of the wing, a stereoscopic camera ( $1280 \times 1024$  pixels) system was used (see Fig. 8). The enclosed angle between two camera viewing

axes was approximately  $90^\circ$ , ensuring optimum measurement accuracy.<sup>10</sup> However, such a camera setup could not make the whole upper surface of the wing within focus for both cameras. The out-of-focus images pose a threat to most optical measurements (see Fig. 7). A usual solution to increase the depth of view is to use the Scheimpflug adapter between lens and sensors.<sup>10</sup> A programmable timing unit (PTU) synchronized a flash lamp with the two cameras. Deformation measurements were repeated when the angle of attack (AoA)  $\alpha$  of the airfoil was  $0^\circ$ ,  $2^\circ$ ,  $4^\circ$ ,  $6^\circ$ ,  $8^\circ$ ,  $10^\circ$ , respectively. For each AoA, the free stream velocity  $u_\infty$  was gradually increased from 0 to 8 m/s to avoid too large displacements. At each flow condition, the programmable timing unit controlled the synchronization between the flash lamp and cameras. Finally, we got two image series for both cameras for each flow condition. More information about the experimental setup is in earlier work.<sup>20</sup>

#### 5. Experimental results

##### 5.1. Optical flow for airfoil deformation measurements

Because the largest pattern displacement due to wing deformation between wind off (0 m/s) and wind on (8 m/s) was greater

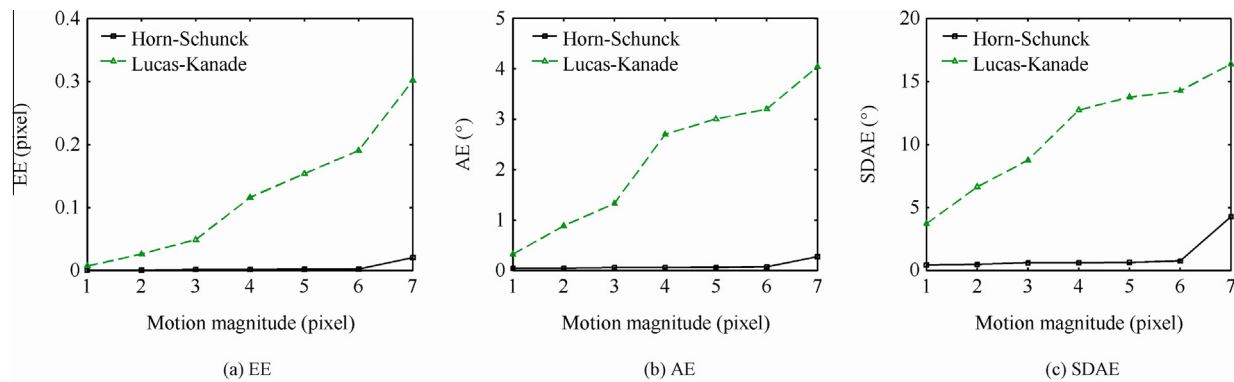


Fig. 6 Errors with increasing motion magnitude.

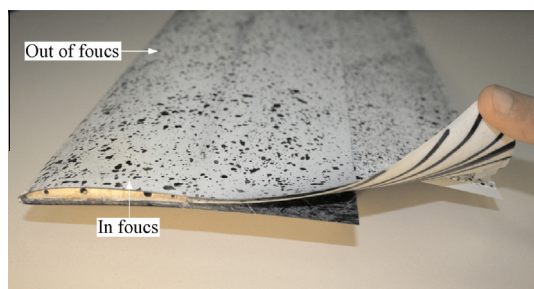


Fig. 7 Flexible birdlike airfoil.

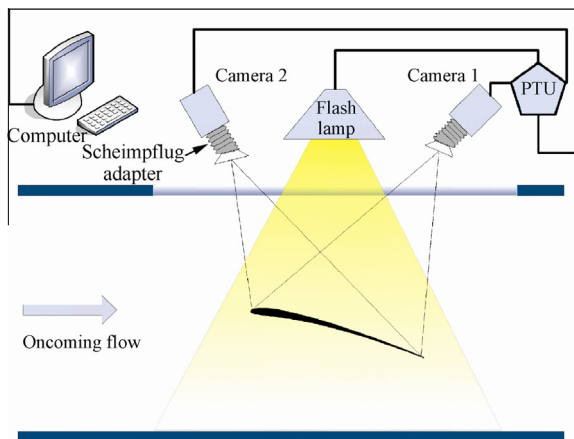


Fig. 8 Stereo camera setup.

than 6 pixels, the HS optical flow would not yield accurate results as demonstrated before. In consequence, the deformation was determined between 0 m/s to 5 m/s, 5 m/s to 7 m/s, and 7 m/s to 8 m/s. At each data point, the flexible shells of the wing deflected steadily and 30 images were taken. The post processing process of these images was the same as the LK method.<sup>20</sup> A simple average strategy, a histogram stretching and a Gaussian filter were successively applied to recorded images to enhance their quality. Then, for each camera, the optical flow between images of aforementioned neighboring velocities was calculated by HS and added up to get the final optical flow. Finally, each camera generated an optical flow

field estimating the airfoil deformation in images between 0 m/s and 8 m/s. It is noted that all the parameters were kept the same as before except that the inner warping iteration was reduced to 3, which demonstrates the more robustness of HS than LK whose parameters have to be tuned carefully for different input images.<sup>20</sup>

Two images taken by two cameras when AoA of the airfoil was 8° at wind off are shown in Fig. 9(a1) and Fig. 9(a2). It is worth noting that the airfoil was not homogeneously illuminated, and that is why a histogram stretching was carried out.

For the airfoil at 8°, two HS optical flow fields between 0 m/s and 8 m/s for the two corresponding cameras can be seen in Fig. 9(b1) and (b2). As before, the optical flow was coded by the color wheel (see Fig. 1(b)). Not only sharp discontinuities were preserved, but also the gaps between overlapping flexible shells were captured. However, it is interesting to see that LK captured a more noticeable gap, see Fig. 9(c1) and (c2). This can be explained by the image-driven anisotropic diffusion tensor used in LK optical flow. Actually, as the air flow ran across the wing almost evenly, the overlapping shells deformed almost the same along the spanwise direction. The deformation difference of the gap and the shell was not so obvious, which can be indicated by the construction of the airfoil (see Fig. 7). As a result, we assume that the HS optical flow in gap regions was more realistic. To illustrate the difference of HS and LK in motion boundary, the enlarged views of Square 1 and Square 3 (the green squares in Fig. 9(a1) and (a2)) are shown in Fig. 9(a-3-1) and (a-3-3), respectively. As expected, the optical flow of HS (Fig. 9(b-3-1) and (b-3-3)) preserved an obviously much better velocity discontinuity than that of LK (Fig. 9(c-3-1) and (c-3-3)). At the same time, HS showed higher sensitivity to noise compared to LK (see Fig. 9(b-3-2), (b-3-4), (c-3-2) and (c-3-4)). The square 2 in Fig. 9(a1) represents a low motion displacement region where the noise was dominated by random vibration of the airfoil and none homogenous illumination. Square 4 in Fig. 9(a2) represents a high specular reflection region, which resulted from the aluminum frame where the noise was dominated by the violation of intensity constancy assumption. The velocity range for images from camera 1 was  $U_1 \in [-0.66, 2.70]$  pixels,  $V_1 \in [-4.47, 1.51]$  pixels, while the velocity range for images from camera 2 was  $U_2 \in [-16.31, 1.70]$  pixels and  $V_2 \in [-2.78, 2.41]$  pixels.

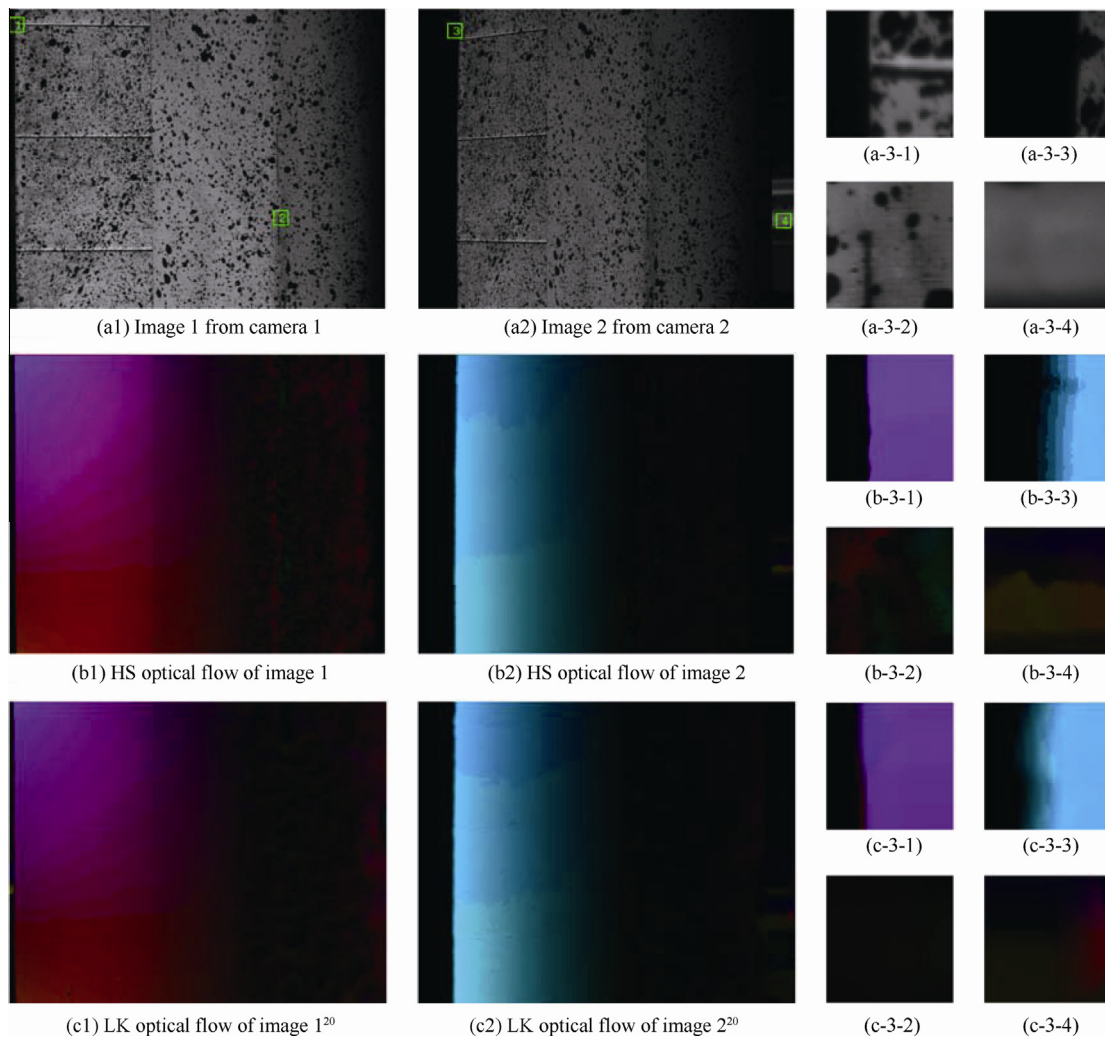


**Fig. 9** Airfoil images ( $\alpha = 8^\circ$ ,  $u_\infty = 0$  m/s) and corresponding optical flow fields ( $\alpha = 8^\circ$ ,  $u_\infty = 0-8$  m/s).

### 5.2. Airfoil vertical deformation

After camera calibration, the 3-D velocity field can be calculated by the stereo optical flow fields. Because the Scheimpflug condition was used in experiments to increase the depth of view, the image plane and the lens plane were not parallel anymore, accordingly, and the polynomial model<sup>34</sup> rather than the pinhole model was used to calibrate cameras. The polynomial had a cubic dependence in  $x$  and  $y$ , but a quadratic dependence in  $z$ . The calibration grid was inclined with the same angle of the chord line of the airfoil and was translated to three  $z$  positions with an interval of 10 mm, containing the whole range of airfoil deformation. Once cameras were calibrated, the correspondence between a point of the real world and two pixels of two stereo images was recovered. Combining two optical flow fields according to the method proposed by Soloff et al.,<sup>34</sup> we could calculate the 3-D displacement of the wing.

As the SG04 airfoil during wind on deforms in a 2-D way, the vertical deformation predominates the 3-D displacements. This vertical deformation  $dz$  calculated by HS is shown by a contour graph in Fig. 10(a). The result was nondimensionalized by the chord length  $c$ . Compared with the result of LK

(see Fig. 10(b)), HS illustrated a smoother flow field in the flexible shells (deformed region), which was the actual situation as discussed before. LK captured the gaps between overlapping shells more clearly than HS. However, as mentioned before, the patterns of the flow field of LK in the flexible shells were mostly induced by the image-driven anisotropic diffusion process where the local texture and local motion was not consistent. In the near-zero deformation region, HS showed more fluctuation than LK, which was mainly the result of none homogenous illumination. Again, it is demonstrated that HS was more sensitive to noise than LK. However, it should be remembered that HS generated 100% dense flow field while LK could not because a Gaussian integration window (22 pixels) was utilized by LK<sup>20</sup> (see Eq. (8)). The HS result was also compared with the traditional image correlation result (see Fig. 10(c)). Apparently, the image correlation result was much smoother than both optical flow results, which was under expectation because a large interrogation window (from  $128 \times 128$  pixels down to  $32 \times 32$  pixels, with 50% overlap) was used during image correlation calculations.<sup>20</sup> Smaller interrogation windows were tested before calculations, but the results showed that a window size of  $32 \times 32$  pixels



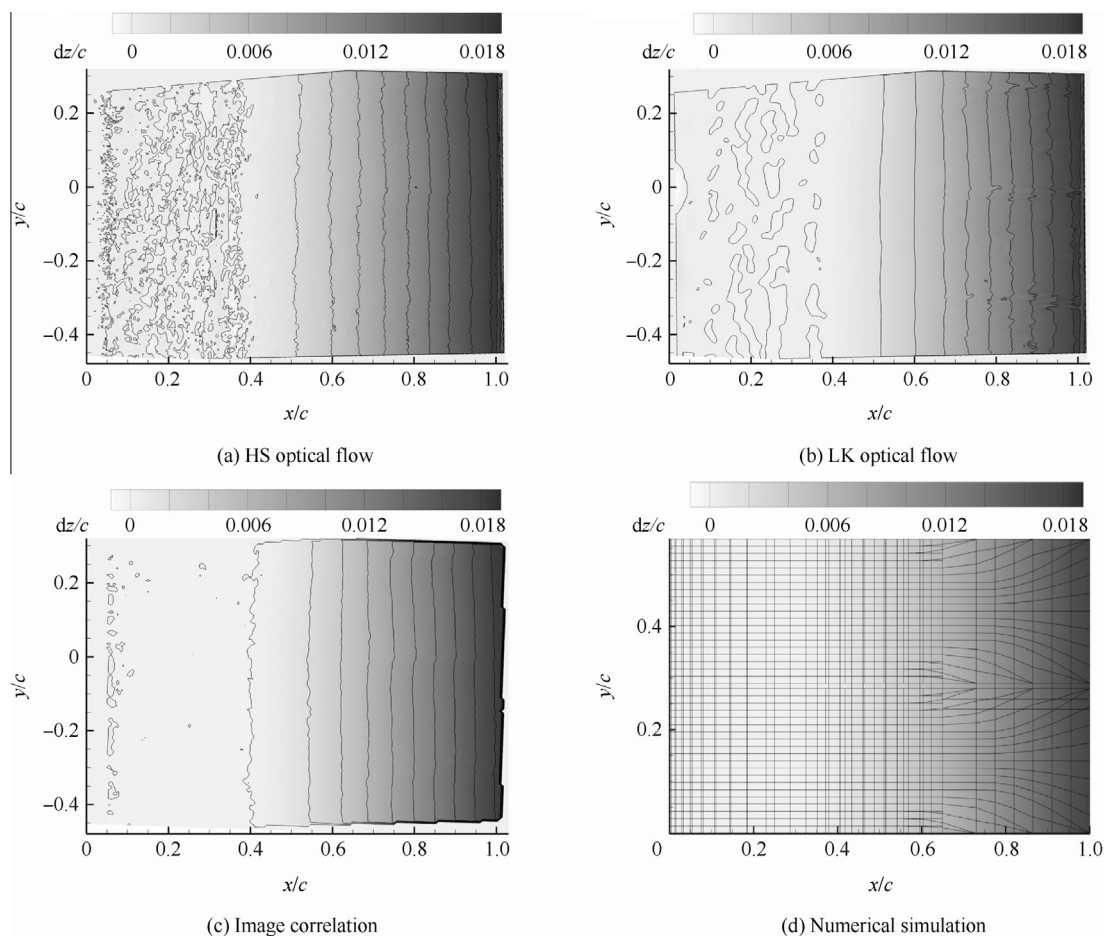


**Fig. 10** Vertical deformation of different methods ( $\alpha = 8^\circ$ ,  $u_\infty = 0\text{--}8$  m/s).

provided the best compromise between spatial resolution and accuracy. Therefore, image correlation will fail to capture motion details and tend to blur motion boundaries because its resolution is confined by the interrogation window size. A sharp motion boundary of the image correlation result shown in Fig. 10(c) does not result from the image correlation method but from a manually defined polygon mask that fits the outline of the airfoil in images. Finally, the HS result was compared with the numerical simulation result (see Fig. 10(d)). It is noted that the lines in Fig. 10(d) represent finite-element model used in the structural part of the simulation rather than contour lines. The numerical simulation was based on solving the fluid–structural interaction (FSI) problem by a partitioned coupling approach where the fluid and structural solvers are linked together in a well-validated coupling environment with the aid of flexible data transfer libraries.<sup>20</sup> The deformation contour of FSI showed good agreement with that of HS, LK and image correlation.

To further show the difference between the results of HS, LK, image correlation and FSI, a slice was cut at  $y/c = -0.0825$  of three experimental results in Fig. 10 along the chord line, while a slice was cut at the horizontal midline of the FSI result. The vertical deformation curves of different methods are shown in Fig. 11(a). All these curves are consistent with each other. The deformation of the wing starts

around  $0.38c$  from the leading edge, displays an exponential-like increase and reaches the peak value around  $0.018c$ . Three experimental curves show small oscillation only when  $dz/c$  was close to zero. Again, the HS result showed the biggest fluctuation in the near-zero deformation region. The advantage of HS over LK in motion-discontinuity preservation can still be seen around  $x/c = 1$  in Fig. 11(a), where the deformation curve of HS dropped down more sharply than the curve of LK. However, this advantage is not so obvious because of the small scale of this motion-blur region compared to the image size. From another perspective, this also proves the applicability of LK optical flow in this experiment, despite the not so overwhelming power in preserving the motion boundary, compared to HS.

Finally, HS method was applied to images of the whole series of AoA. HS optical flow fields and the corresponding 3-D vertical deformation contours were calculated, respectively. Then, the trailing edge deflections for each AoA were recovered. The deflections calculated by HS were illustrated in Fig. 11(b), together with the results of LK and FSI. The results of HS and LK show a perfect match, which demonstrates that both of HS and LK are capable of capturing large deformation of the wing accurately. Both optical flow results are in good agreement with FSI results except for the strayed value at  $0^\circ$ , where the numerical simulation overestimates the experimental

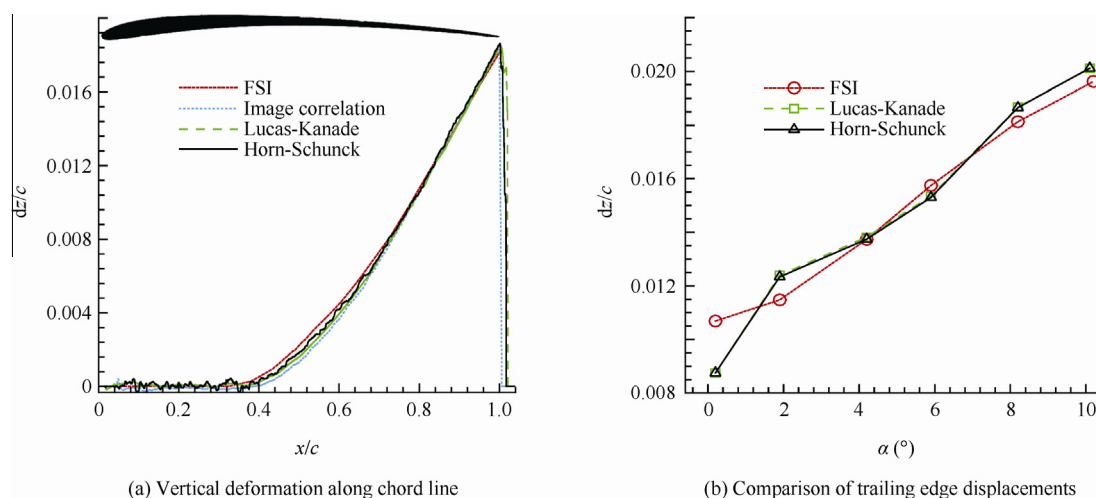


Fig. 11 Vertical deformation curves and trailing edge displacements.

value. A reasonable linear correlation between the trailing edge deflection and angle of attack can be demonstrated in Fig. 11 (b).

## 6. Conclusions

- (1) An improved Horn–Schunck optical flow technique is developed in this paper and the method is applied to measuring the static airfoil deformation at different AoAs in a wind tunnel.
- (2) The HS method is validated on synthetic images and compared with a Lucas–Kanade optical flow technique. The HS method displays a better convergency. With increasing displacements in images, the HS technique shows constantly better performance, especially in the motion boundary region. The maximum permissible displacement for the HS method is proved to be 6 pixels, twice the value of the LK technique.
- (3) The HS method is utilized to calculate optical flow in images induced by the airfoil deformation and compared with the LK method. The HS technique shows higher sensitivity to noise within near-zero deformation regions (the stiff fore part of the airfoil) but generates sharper motion boundaries and offers higher robustness within deformation regions (the flexible rear part of the airfoil).
- (4) The 3-D deformation of the airfoil is reconstructed from the stereo HS optical flow fields. The results of HS agree well with the results of LK and image correlation. The HS method possesses the highest spatial resolution (single pixel), followed by the LK method (integration window size) and the image correlation method (interrogation window size). LK and image correlation show greater performance to resist noise, while the advantage of HS over LK and image correlation is to preserve the motion detail and the motion discontinuity.
- (5) Despite the small differences, experimental measurements display a good match with numerical results calculated by a fluid–structure interaction simulation.

Therefore, it is concluded that optical flow can be applied in airfoil deformation measurements. Future work will apply

optical flow to measure the precisely controlled deformations, which can offer a better insight into the accuracy of the presented method.

## References

1. Brooks JD, Beamish JK. *Measurement of Model Aeroelastic Deformations In The Wind Tunnel At Transonic Speeds Using Stereo Photogrammetry*. Washington, D.C.: NASA Langley Research Center; 1977, Report No.: NASA-TP-1010.
2. Lunsford N, Jacob J. High speed videogrammetry of flexible wings in flapping flight. *47th AIAA aerospace sciences meeting including the new horizons forum and aerospace exposition*. Reston: AIAA; 2009. p. 1–14.
3. Burner AW, Radeztsky RH, Liu T. Videometric applications in wind tunnels. In: Bellingham V, editor. *Proceedings of SPIE 3174, videometrics*. SPIE; 1997. p. 234–47.
4. Graves S, Burner A, Edwards J, Schuster D. Dynamic deformation measurements of an aeroelastic semispan model. *J Aircr* 2003;40(5):977–84.
5. Chakravarthy A, Albertani R, Gans N, Evers J. Experimental kinematics and dynamics of butterflies in natural flight. *47th AIAA aerospace sciences meeting including the new horizons forum and aerospace exposition*. Reston: AIAA; 2009. p. 1–12.
6. Asme T, Guard O, Rao KR, Bunce R. A stereo videogrammetry system for monitoring wind turbine blade surfaces during structural testing. *ASME early career technical conference*. New York: ASME; 2009. p. 1–10.
7. Liu TS, Montefort J, Gregory J, Palluconi S, Crafton J, Fonov S. Wing deformation measurements from pressure sensitive paint images using videogrammetry. *41st AIAA fluid dynamics conference and exhibit*. Reston: AIAA; 2011. p. 1–31.
8. Baumann PH, Butefisch KA. Measurement of hinge moments and model deformations in wind tunnels by means of moiré interferometry. *Proceedings of SPIE 2546, optical techniques in fluid, thermal, and combustion flow*. Bellingham: SPIE; 1995. p. 16–32.
9. Leifer J, Black JT, Smith SW, Ma N, Lumpkin JK. Measurement of in-plane motion of thin-film structures using videogrammetry. *J Spacecr Rockets* 2007;44(6):1317–25.
10. Raffel M, Willert C, Kompenhans J. *Particle image velocimetry: a practical guide*. 2nd ed. Berlin: Springer; 2007. p. 79–226.
11. Thomas W, Robert K, Erlinghagen T, Wagner H. Shape and deformation measurement of free flying birds in flapping flight. In: Tropea C, Bleckmann H, editors. *Nature-inspired fluid mechanics*. Berlin: Springer; 2012. p. 135–48.

12. Schmidt T, Tyson J, Galanulis K. Full-field dynamic displacement and strain measurement using advanced 3D image correlation photogrammetry: part 1. *Exp Technol* 2003;**27**(3):47–50.
13. Siebert T, Neumann I. High-speed digital image correlation: error estimations and applications. *Opt Eng* 2007;**46**(5):051004.
14. Lawson M, Sirohi J. Measurement of deformation of rotating blades using digital image correlation. *52nd AIAA/ASME/ASCE/AHS/ASC structures, structural dynamics and materials conference*. Reston: AIAA; 2011. p. 1–15.
15. Jennings A, Black J. Texture-based photogrammetry accuracy on curved surfaces. *AIAA J* 2012;**50**(5):1060–71.
16. Barron JL, Fleet DJ, Beauchemin SS. Performance of optical flow techniques. *Int J Comput Vis* 1994;**12**(1):43–77.
17. Horn BKP, Schunck BG. Determining optical flow. *Artif Intell* 1981;**17**(1–3):185–203.
18. Lucas BD, Kanade T. An iterative image registration technique with an application to stereo vision. *Proceedings of the 7th international joint conference on artificial intelligence*. San Francisco: Morgan Kaufmann Publishers Inc.; 1981. p. 674–9.
19. Bruhn A, Weickert J, Schnörr C. Lucas/Kanade meets Horn/Schunck: combining local and global optic flow methods. *Int J Comput Vis* 2005;**61**(3):1–21.
20. Gong XL, Bansmer S, Strobach C, Unger R, Haupt M. Deformation measurement of a birdlike airfoil with optical flow and numerical simulation. *AIAA J* 2014;**52**(12):2807–16.
21. Baker S, Scharstein D, Lewis JP. A database and evaluation methodology for optical flow. *Int J Comput Vis* 2011;**92**(1):1–31.
22. Nagel HH. Constraints for the estimation of displacement vector fields from image sequences. *International Joint Conference on artificial intelligence*. San Francisco: Morgan Kaufmann Publishers Inc.; 1983. p. 945–51.
23. Black MJ, Anandan P. A framework for the robust estimation of optical flow. *4th International conference on computer vision*. Piscataway, NJ: IEEE Press; 1993. p. 231–6.
24. Brox T, Papenberger N, Weickert J. High accuracy optical flow estimation based on a theory for warping. *8th European conference on computer vision*. Berlin: Springer; 2004. p. 25–36.
25. Zach C, Pock T, Bischof H. A duality based approach for realtime TV-L 1 optical flow. *29th DAGM symposium*. Berlin: Springer; 2007. p. 214–23.
26. Brox T, Weickert J. Nonlinear matrix diffusion for optic flow estimation. *24th DAGM symposium*. Berlin: Springer; 2002. p. 446–53.
27. Xiao JJ, Cheng H, Sawhney H. Bilateral filtering-based optical flow estimation with occlusion detection. *9th European conference on computer vision*. Berlin: Springer; 2006. p. 211–24.
28. Sand P, Teller S. Particle video: long-range motion estimation using point trajectories. *Int J Comput Vis* 2008;**80**(1):72–91.
29. Westerweel J. Efficient detection of spurious vectors in particle image velocimetry data. *Exp Fluids* 1994;**16**(3–4):236–47.
30. Sun DQ, Roth S, Black MJ. Secrets of optical flow estimation and their principles. *IEEE computer society conference on computer vision and pattern recognition*. Piscataway, NJ: IEEE Press; 2010. p. 2432–9.
31. Bouguet J. *Pyramidal implementation of the Lucas Kanade feature tracker description of the algorithm*. Santa Clara, CA: Intel Corporation, Microprocessor Research Labs; 1999. p. 1–9.
32. Galvin B, McCane B, Novins K, Mason D, Mills S. Recovering motion fields: an evaluation of eight optical flow algorithms. *British machine vision conference*. Manchester: BMVC; 1998. p. 195–204.
33. Bansmer S, Buchmann N, Radespiel R, Unger R, Haupt M, Horst P, et al. Aerodynamics and structural mechanics of flapping flight with elastic and stiff wings. In: Bleckmann H, Tropea Ca, editors. *Nature-inspired fluid mechanics*. Berlin: Springer; 2012. p. 331–54.
34. Soloff SM, Adrian RJ, Liu ZC. Distortion compensation for generalized stereoscopic particle image velocimetry. *Meas Sci Technol* 1997;**8**(12):1441–54.

**Gong Xiaoliang** is a Ph.D. student at School of Aeronautics, Northwestern Polytechnical University. He received his B.S. degree from the same university in 2010. During his joint-Ph.D. program, he studied at Institute of Fluid Mechanics, Technische Universität Braunschweig (Germany). His main research interests are optical measurement techniques for motion, shape and deformation in wind tunnels.

**Stephan Bansmer** is the head of the research group “Multiphase Flow and Icing” at Institute of Fluid Mechanics, Technische Universität Braunschweig (Germany). He received his Ph.D. degree from the same university in 2010. During his assignments at McGill University (Canada), Ecole Nationale Supérieure de l’Aéronautique et de l’Espace (France) and Airbus France, he gained experience in both experimental and computational methods in fluid mechanics.